



Tailored poly-heptazine units in carbon nitride for activating peroxymonosulfate to degrade organic contaminants with visible light

Hongbo Ming^a, Peiyun Zhang^a, Yang Yang^a, Yu Zou^{a,b}, Can Yang^a, Yidong Hou^{a,*}, Kaining Ding^{a,b,**}, Jinshui Zhang^a, Xinchun Wang^{a,*}

^a State Key Laboratory of Photocatalysis on Energy and Environment, College of Chemistry, Fuzhou University, Fuzhou 350108, PR China

^b Fujian Provincial Key Laboratory of Electrochemical Energy Storage Materials, College of Chemistry, Fuzhou University, Fuzhou 350108, PR China

ARTICLE INFO

Keywords:

Carbon nitride
Photocatalytic
Peroxymonosulfate activation
Electronic structure
Organic removal

ABSTRACT

The photocatalytic peroxymonosulfate (PMS) activation process offers great potential for organic wastewater treatment. In this study, enol-incorporated carbon nitride (ECN) catalysts were used for PMS activation to degrade organic pollutants under visible-light irradiation. Our experimental and theoretical results revealed that the incorporation of enol into the poly-heptazine-based carbon nitride framework effectively tuned the electronic structure. The obtained ECN showed promoted PMS activation capability, along with increased visible-light harvesting ability and improved photogenerated charge separation. As a result, an excellent performance with a bisphenol A removal rate of 100% within 20 min and a total organic carbon (TOC) removal rate of 86% in 30 min was achieved in the Vis-PMS/ECN process. This was because ECN functioned as an efficient photocatalyst as well as PMS activator, which enabled the PMS activation process to proceed smoothly for $\bullet\text{SO}_4^-$ production under visible-light irradiation. These findings could offer some guidelines for the development of efficient metal-free photocatalysts in the persulfate-based advanced oxidation process for environmental remediation.

1. Introduction

Sulfate radical-based advanced oxidation processes have gained increasing attention for the deep oxidation of refractory organics in wastewater [1–4]. In comparison to hydroxyl radicals ($\bullet\text{OH}$) produced by the classical Fenton process, sulfate radicals ($\bullet\text{SO}_4^-$) generated from the activation of persulfate have a higher oxidation potential ranging from 2.6 to 3.1 V, longer half-life period (30–40 μs) and wider adaptive working pH scale range (2–8). These factors are favorable for efficiently removing persistent organic pollutants [5,6]. There are many appealing technologies that can activate persulfate to produce $\bullet\text{SO}_4^-$, including thermolysis, sonolysis, photolysis and catalysis [7–11]. Among these, the visible-light-driven photocatalytic activation of persulfate has received significant interest recently, due to its high efficiency and potential utilization of solar energy. The efficiency of the process is closely associated with the visible-light response and the sulfate radical-based Fenton-like reactions [12–14]. Consequently, for the heterogeneous catalytic oxidation process, it is very essential to explore photocatalysts

with superior persulfate activation abilities under visible-light irradiation.

Recently, some semiconductors containing transition metals (e.g., Co-, Mn-, Fe-, and V-) have been used as photocatalysts for persulfate activation and they have exhibited good organic pollutant decomposition performance [15–18]. Nevertheless, these photocatalysts have been greatly restricted in practical water treatment applications due to metallic ion leaching during PMS activation, and they can potentially cause the risk of potential toxicity and secondary pollution. To this end, it is highly desirable to advance metal-free photocatalysts as alternatives for the efficient activation of persulfate.

Graphitic carbon nitride (CN) conjugated by sp^2 hybridized C and N atoms have been extensively studied as metal-free semiconductor photocatalysts for energy and environment applications, including the visible-light-driven activation of persulfate for organic pollutants degradation [19,20]. Nevertheless, the degradation efficiency over pristine CN seriously suffers from fast charge recombination and insufficient activity sites for persulfate activation [21,22]. Therefore, metals,

* Corresponding authors.

** Corresponding author at: State Key Laboratory of Photocatalysis on Energy and Environment, College of Chemistry, Fuzhou University, Fuzhou 350108, PR China.

E-mail addresses: ydhhou@fzu.edu.cn (Y. Hou), dknfzu@fzu.edu.cn (K. Ding), xcwang@fzu.edu.cn (X. Wang).

<https://doi.org/10.1016/j.apcatb.2022.121341>

Received 11 November 2021; Received in revised form 22 February 2022; Accepted 19 March 2022

Available online 25 March 2022

0926-3373/© 2022 Elsevier B.V. All rights reserved.

metal oxides, or metal phosphates nanoparticles with intrinsic catalytic behavior of PMS activation have been loaded onto CN to accelerate charge separation and activate persulfate, and significant improvements in organic pollutant removal have been achieved [23–25]. However, metal species leaching is still unavoidable, and this severely undermines the appealing metal-free characteristics of CN for water treatment [26–28]. Therefore, creating nonmetal-containing reactive sites in CN to promote PMS activation, and speed up charge separation, is of great importance to maintain the metal-free advantages of CN for persulfate activation for water purification.

The incorporation of functional groups into g-C₃N₄ conjugated system by copolymerization is an efficient way to optimize its optical/electronic properties [29,30]. As a kind of enol, acetylacetone contained conjugated structure and hydroxyl group, which facilitated the copolymerization between acetylacetone and urea for preparing carbon nitride. The chromophore centers of enol could improve the light harvesting ability of CN, contributing beneficially to the photocatalytic activity [31–33]. The presence of elemental oxygen with strong electron-withdrawing abilities could induce the delocalization of the π -conjugated electronic system in the enol-incorporated CN framework (ECN), thus a push/pull electron system would be formed in the ECN, which could promote the photogenerated charge separation. Furthermore, the delocalization of π -electrons in ECN would also be advantageous to the PMS adsorption [34]. Upon visible-light irradiation, the photogenerated electrons constantly migrated to adsorbed PMS, enabling the PMS activation process to proceed smoothly. Therefore, we incorporated enol into a CN matrix through the thermal copolymerization of urea and acetylacetone to advance CN for peroxymonosulfate (PMS) activation in this study. As expected, the obtained ECN exhibited an efficient photocatalytic activation of persulfate towards organic pollutant removal under visible-light irradiation. Additionally, the influencing factors for the Vis-PMS/ECN process during BPA degradation were investigated in detail. Moreover, PMS activation mechanism over ECN for the formation of $\bullet\text{SO}_4^-$ was also proposed.

2. Experimental

2.1. Chemicals

Potassium peroxydisulfate (PMS) and bisphenol A (BPA) were purchased from Shanghai Aladdin Biochemical Technology Co., Ltd. (China). Urea, acetylacetone and methanol were obtained from Sinochem Chemical Reagent Co., Ltd. (China). 5, 5-Dimethyl-1-pyrroline-N-oxide (DMPO) and 2,2,6,6-tetramethylpiperidine (TEMP) were provided by J&K Chemical Ltd. All chemicals were used as received without any further purification, and all aqueous solutions were prepared with ultrapure water.

2.2. Synthesis of catalysts

ECN was synthesized by a modified method according to the literature [35]. Typically, a designed amount of acetylacetone (20, 40, 60, 80, 100 μL) was dissolved in 1 mL ethanol. Urea (10 g) and the solution were mixed and grinded in a mortar for 10 min. Then the mixture was calcined at 550 $^{\circ}\text{C}$ for 2 h with a ramping rate of 5 $^{\circ}\text{C min}^{-1}$. The obtained samples were denoted as ECN20, ECN40, ECN60, ECN80, and ECN100, respectively. The pristine CN was also prepared using the same procedure without adding acetylacetone.

2.3. Characterization and DFT calculation method

The samples were examined by X-ray diffraction (XRD) analysis on Bruker D8 Advance XRD equipment with Cu K α radiation ($\lambda = 1.5406 \text{ \AA}$). The morphology and structure was analyzed by field scanning electron microscope (Nova NanoSEM 230) and transmission electron microscopy (TEM TECNAI G2 F20). Fourier-transform infrared (FTIR)

spectra were carried out by NICOLET IS50 (Thermo SCIENTIFIC). X-ray photoelectron spectrum (XPS) was recorded on a PHI Quantum 2000 XPS with the C1s peak (284.6 eV) as a reference. Solid-state NMR spectroscopy including ^{13}C CPMAS (Cross Polarization Magic Angle Spinning) and ^{13}C DDMAS (Dipolar Decoupling Magic Angle Spinning) NMR spectra were recorded on Nuclear Magnetic Resonance Spectrometer (600 M). Brunauer-Emmett-Teller specific surface area (SBET) was measured with Micromeritics ASAP 2020 apparatus (USA). UV-Vis diffuse reflectance spectra (DRS) were performed on a Cary 5000 of Agilent Technologies using BaSO₄ as a reference. Photoluminescence (PL) spectra were investigated by a modular fluorescence spectrometer (Fluorolog-3 Horiba). The photoelectrochemical measurement and electrochemical impedance spectroscopy (EIS) were carried out using a potentiostat (Bio-Logic SP-150) with three-electrode configuration, which included the working electrode (CN and ECN60 film), a platinum-mesh counter electrode and Ag/AgCl reference electrode. Electron paramagnetic resonance (EPR) spectra were recorded on a Bruker A300 spectrometer at room temperature. Density functional theory (DFT) calculation was performed using the DMol3 code of the Materials Studio17 software package to optimize the structure [36]. Perdew–Burke–Ernzerhof (PBE) exchange–correlation function of the generalized gradient approximation (GGA) was used to describe the interactions of the electrons [37]. The double numerical plus polarization (DNP) basis set was used for all the models, which was comparable to Pople's 6–31 G* basis set in the Gaussian code [38]. More detail about the DFT calculation was given in Text S1 in [supplementary information](#).

2.4. BPA degradation test

The catalytic degradation of BPA was performed under visible-light irradiation with a 300 W Xe lamp (PLS-SXE300D/UV, Perfect Light technology) with 420 nm cut-off filter. In a typical experiment, 50 mg of catalyst and an aqueous solution of BPA (150 mL, 20 mg L⁻¹) with an initial pH of 6.7 were mixed into a glass flask reactor. The reaction temperature was maintained at 25.0 $^{\circ}\text{C}$ by a circulating water bath. After stirring for 30 min in dark, 40 mg L⁻¹ of PMS was added to the mixture and the system was exposed to visible-light in the meantime. The visible-light (380–780 nm) intensity was 350 mW cm⁻², and the distance between light source and catalysis system surface was controlled as 5 cm. During the reaction, 0.5 mL of sample was taken and immediately filtrated with a 0.22 μm polyethersulfone membrane at each regular interval for analysis. Then 0.5 mL of methanol was added to the sample for the quenching of the residual PMS. All the control experiments were operated under similar conditions.

BPA concentration in the samples was analyzed by HPLC (1260 infinity Agilent Technologies) analysis at 224 nm equipped with Waters SunFire C18 column. The temperature of the column was set to 25 $^{\circ}\text{C}$. The mobile phase comprised of methanol and deionized water (V: V=70:30) with a flow rate of 1 mL min⁻¹. The injection volume was set as 10 μL . The total organic carbon (TOC) in the BPA solution without adding methanol as the quencher for PMS was analyzed with a Shimadzu TOC-VCPH analyzer.

3. Results and discussion

3.1. Structure and morphology

The physicochemical properties of the synthesized catalysts were systematically investigated. The X-ray diffraction (XRD) patterns (Fig. S1a) showed that all the samples had the characteristic diffraction peaks corresponding to the (100) and (002) planes at 13.0 $^{\circ}$ and 27.3 $^{\circ}$, respectively. These originated from the in-plane structural packing motif of the heptazine units and the interlayer-stacking of the conjugated aromatic system [39]. These two peaks gradually became broader with increasing acetylacetone content in the starting materials, indicating

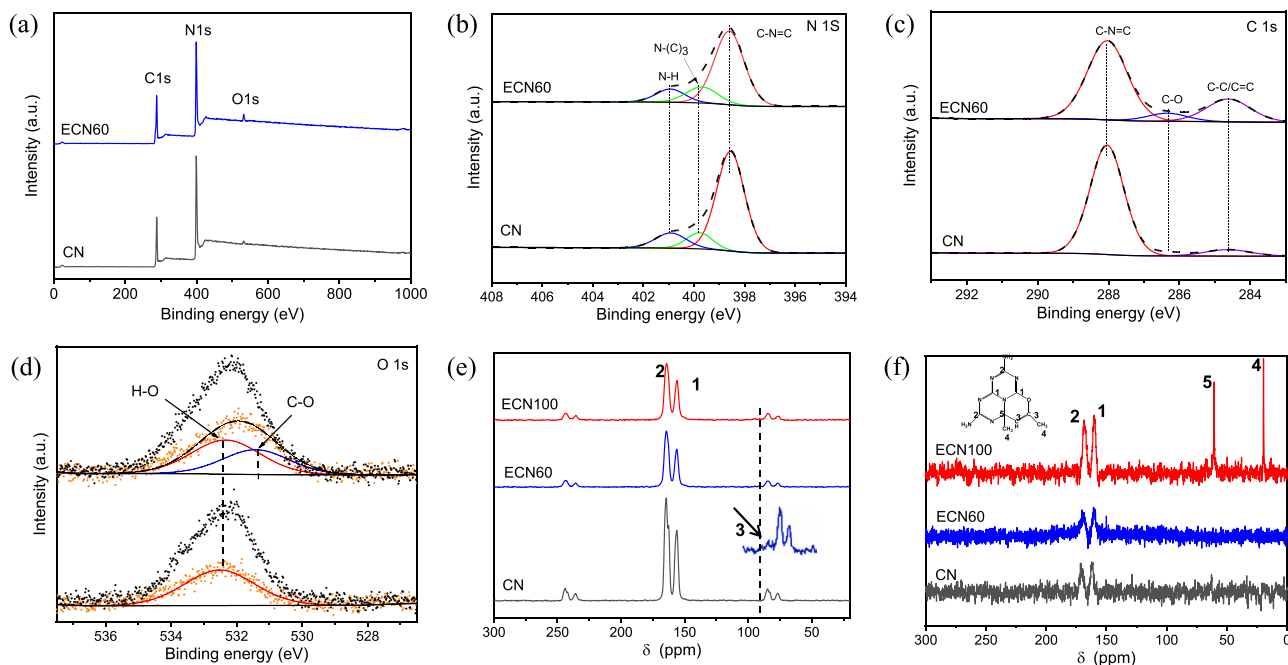


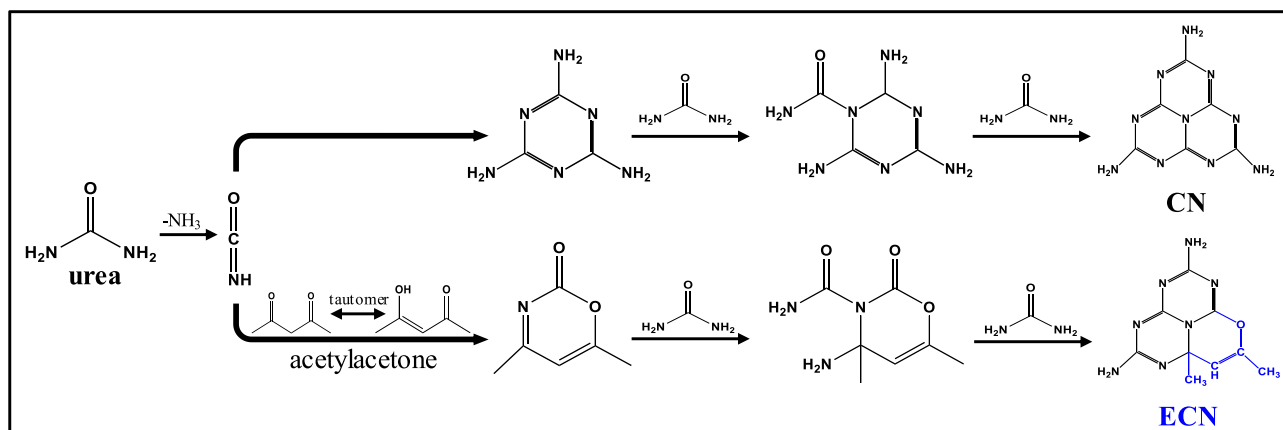
Fig. 1. (a) XPS survey spectra and (b, c and d) deconvolution of N1s, C1s and O1s as shown in the XPS spectra for CN and ECN60. ^{13}C solid-state (e) CPMAS and (f) DDMA NMR spectra for CN, ECN60, and ECN100.

that the addition of acetylacetone resulted in some structural disorder. Fourier transform infrared spectroscopy (FTIR) spectra (Fig. S1b) displayed typical characteristic vibrations for CN, including s-triazine ring vibration at 809 cm^{-1} and the vibration bands for aromatic C-N heterocycles from 1200 to 1600 cm^{-1} [40,41]. These findings indicated that the chemical framework of CN was well maintained after incorporating enol in the poly-heptazine units of the CN materials.

The morphologies and nanostructures of the synthesized catalysts were studied using scanning electron microscopy (SEM) and transmission electron microscopy (TEM). As shown in Fig. S2, both CN and ECN60 displayed a typical stacked sheet-like structure with a porous surface. This was consistent with the specific morphology of carbon nitride derived from urea [42]. The N_2 -sorption isotherms exhibited an H3-type hysteresis loop at relative pressures of 0.8 – 1.0 , indicative of a mesoporous structure (Fig. S3) [43]. Additionally, CN and ECN60 had comparable BET specific surface areas ($90\text{ m}^2\text{ g}^{-1}$ vs. $84\text{ m}^2\text{ g}^{-1}$). These results revealed that incorporating enol in the CN matrix did not induce noticeable texture changes.

Elemental analysis, X-ray photoelectron spectroscopy (XPS) and Solid-state ^{13}C NMR spectroscopy were carried out to confirm the

successful incorporation of enol into the CN matrix. As shown in Table S1, the C content in ECN60 (33.9%) is comparable to that in CN (33.8%). In addition, O atom content increased from 5.1% for CN to 7.6% for ECN60, while N atom content decreased from 60.9% for CN to 57.9% for ECN60. The compositional content differences between CN and ECN60 suggested the partial substitution of N atoms with O atoms in ECN60. The XPS survey spectra showed that the samples contained C, O and N (Fig. 1a). In the high-resolution N 1s spectra (Fig. 1b), three distinct peaks for CN and ECN60 were located at binding energies of 398.5 , 399.8 and 400.9 eV , which were ascribed to the sp^2 -hybridized nitrogen in aromatic triazine rings, tertiary nitrogen and amino groups, respectively [34]. The C 1s spectra (Fig. 1c) was deconvoluted into three peaks: 284.6 , 286.3 and 287.9 eV , which originated from C-C/C=C, sp^2 -hybridized carbon (N=C-N) and C-O, and the peak for C-O bond was obviously observed in ECN60 [44]. The ratio of (C-O)/(N=C-N) was estimated to be 0.10 based on their peak area. In the O 1s spectra (Fig. 1d), both samples had a broad peak at 532.5 eV , which mainly corresponded to adsorbed water. To exclude the effect of surface adsorbed water, we conducted Ar-GCIB (gas cluster ion beam) depth profiling. Notably, ECN60 displayed an extra peak at 531.7 eV , assigned



Scheme 1. Possible reaction process for urea and acetylacetone during thermal polymerization.

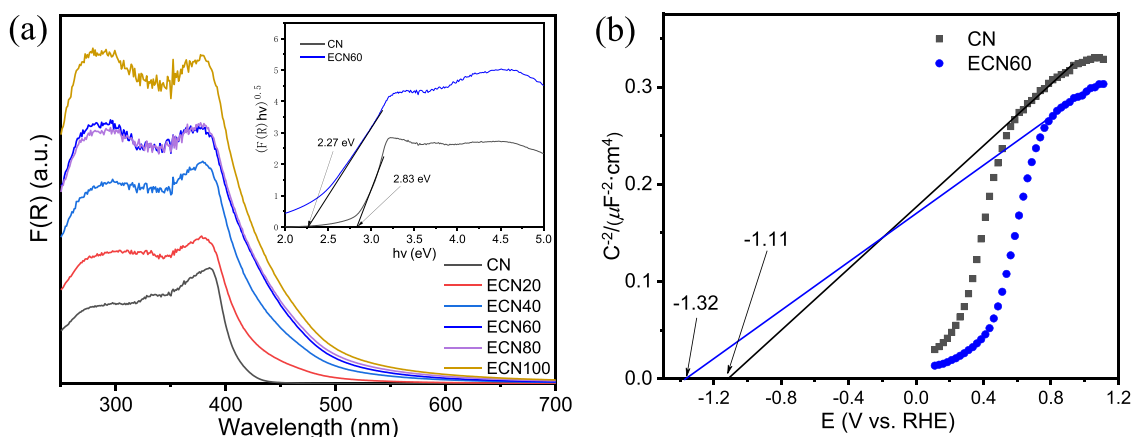


Fig. 2. (a) UV-Vis diffuse reflectance spectra (inset: Tauc plots) and Mott-Schottky plots for the samples.

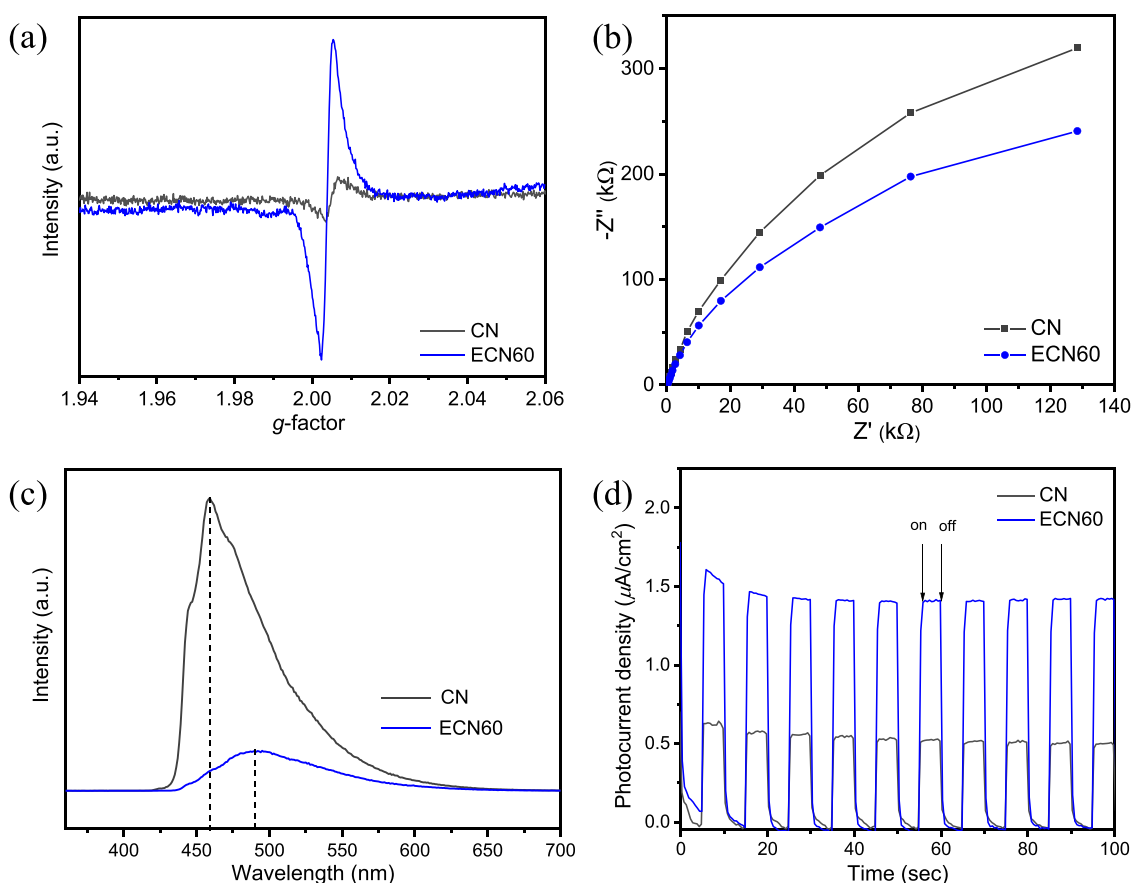


Fig. 3. (a) EPR spectra, (b) EIS Nyquist plots, (c) steady-state photoluminescence spectra, and (d) periodic on/off photocurrent responses for the samples.

to C-O bond [33]. The results implied that O atoms were bonded to carbon atoms in the thermal copolymerization of urea and acetylacetone [35]. Solid-state ^{13}C NMR spectroscopy was used to further reveal the chemical structure of carbon. As shown in Fig. 1e, two dominant peaks centered at 156.1 and 164.6 ppm were assigned to C-N₃ (1) and CN₂-NH₂ (2) in the triazine ring of pristine CN. Compared to CN, ECN60 and ECN100 had a new peak at 96 ppm attributed to -C=C- (3) [45,46]. In the solid-state ^{13}C DDMAS NMR spectra (Fig. 1f), ECN100 presented two novel peaks at 20 and 60 ppm, which correlated to -CH₃ (4) and -N-C- (5), respectively [47]. These two peaks were negligibly observed in ECN60, which could be attributed to the smaller quantity of enol. Considering the above results, it could be deduced that acetylacetone

participated in the thermal polymerization process. This process involved the nucleophilic addition between the tautomer of acetylacetone and cyanic acid as a result of urea decomposition, followed by dehydration reactions proceeded at high temperatures, which finally produced ECN (Scheme 1).

3.2. Optical and electronic properties

The optical properties of the synthesized catalysts were investigated by UV-Vis diffuse reflectance spectrum (DRS). As shown in Fig. 2a, compared to CN, ECN exhibited a gradual red-shift in the light absorption edge with increasing amount of acetylacetone in the starting

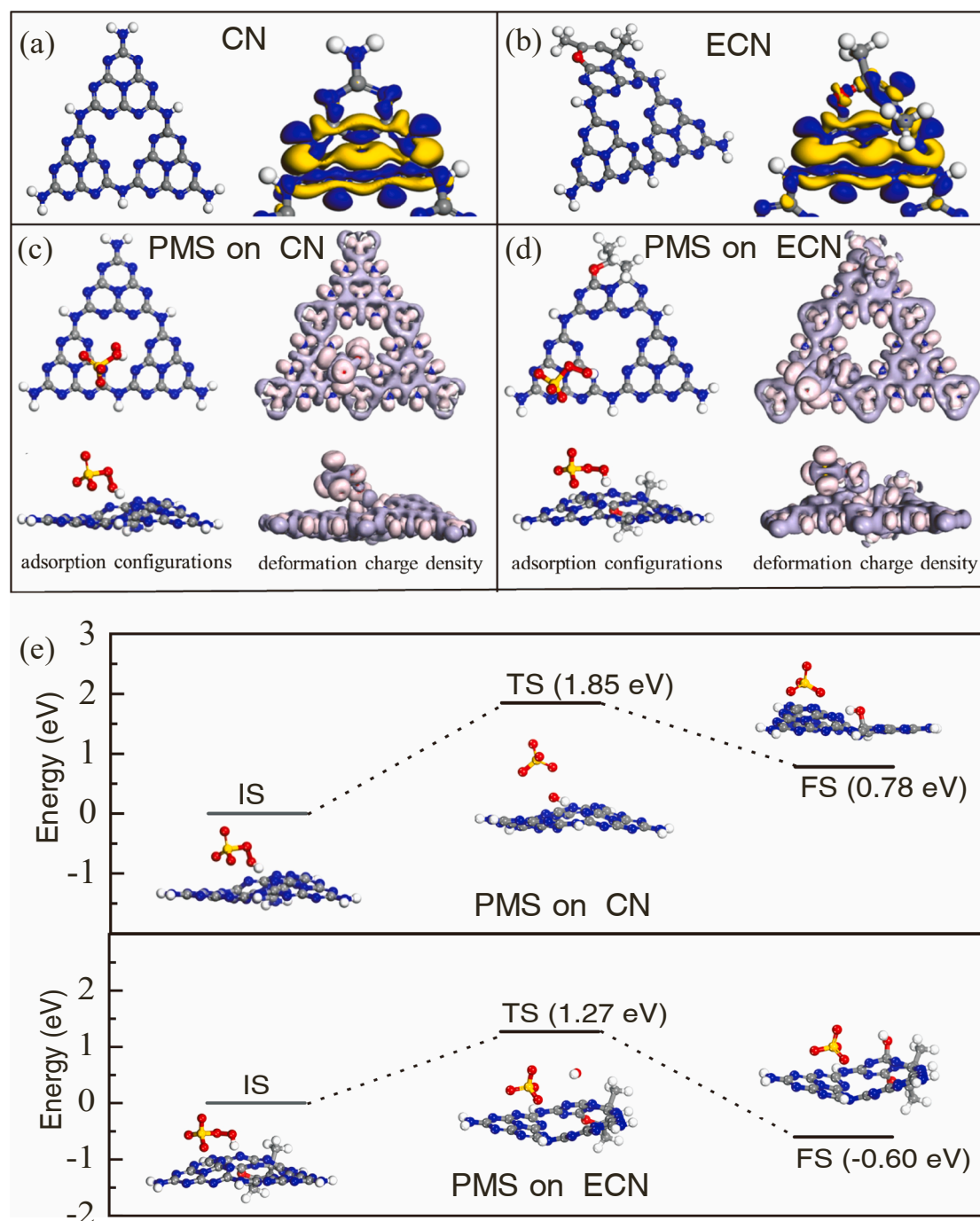


Fig. 4. (a, b) Optimized polymeric trimer models and electron densities of CN and ECN, (c, d) optimal adsorption configurations and deformation charge densities of PMS adsorbed on CN and ECN. (e) Activation pathways of PMS on CN and ECN.

materials. The bandgap energies of CN and ECN60 were estimated by the Kubelka–Munk plots [24,31], and the values were 2.83 eV and 2.27 eV for CN and ECN60, respectively (inset in Fig. 2a). Thus, ECN could harvest more photons in the visible-light spectrum, which would be beneficial for photocatalytic reactions. Fig. 2b shows that both CN and ECN60 were identified as *n*-type semiconductors based on the positive slope of the Mott-Schottky plots. Because the conduction band (CB) of the *n*-type semiconductor was located at a position near the flat band [48], the CB potentials were ca. -1.11 and -1.32 V vs. RHE for CN and ECN60, respectively. The detailed about the energy-level diagram for CN and ECN60 is depicted in Fig. S4, illustrating the narrower band gap and the up-shift in band position of ECN60. The unpaired electrons

in CN and ECN60 were studied using electron paramagnetic resonance (EPR) measurement. Fig. 3a shows that both samples had an EPR signal at a *g*-factor of 2.004, which corresponded to the unpaired electrons in the π -conjugated system [49]. Compared to CN, ECN60 had a much stronger EPR intensity, indicating that more unpaired electrons were present after the enol was incorporated into the CN network. Additionally, the electrochemical impedance spectra (Fig. 3b) showed that ECN60 had a smaller arc radius than CN, indicative of a higher mobility for charge transfer [50]. The incorporation of enol into the CN network could also effectively modulate the electronic structure. Therefore, enhanced PMS activation performance under visible-light irradiation would be highly anticipated.

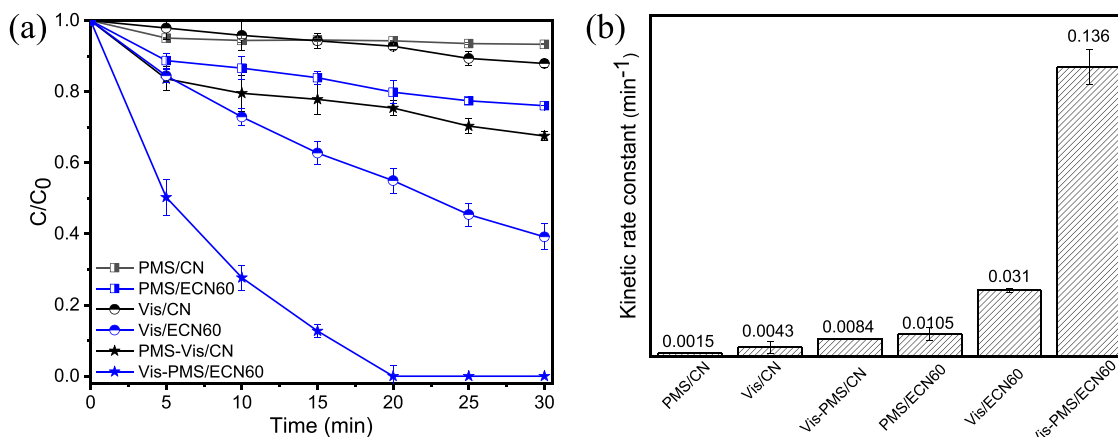


Fig. 5. (a) BPA removal and (b) the first order-kinetic constants for the different processes. Reaction conditions: [PMS] = 40 mg L⁻¹; [Catalyst] = 0.33 g L⁻¹; [BPA] = 20 mg L⁻¹; T = 25 °C.

The photogenerated carrier recombination and separation behavior of the catalysts was analyzed by steady state photoluminescence (PL) spectroscopy. As shown in Fig. 3c, the PL emission of ECN60 was significantly diminished compared to CN, indicating substantial inhibition of electron-hole recombination in ECN60. Additionally, the emission peak showed a red-shift from 460 to 490 nm, which was in good agreement with the narrower bandgap of ECN60 [51]. Photoelectrochemical measurements (Fig. 3d) were also carried out to further characterize the photogenerated charge behavior of the samples. The photocurrent of ECN60 was much higher than that of CN, indicating a remarkable improvement in the charge transfer dynamics. These results clearly demonstrated that the incorporation of enol into the CN matrix promoted the charge separation and transfer.

To obtain more insightful information about electronic structure tailoring through the incorporation of enol into the CN network, we conducted DFT calculations for polymeric trimer models of CN and ECN. Fig. S5 shows that the highest occupied molecular orbital (HOMO) and lowest unoccupied molecular orbital (LUMO) electronic structures changed considerably when CN was incorporated with enol, and ECN had an up-shift in the positions of the orbitals and a narrower bandgap (Fig. S6), which was consistent with the optical and electrochemical measurement results. Specifically, the up-shift in the LUMO of ECN thermodynamically facilitated the transfer of photogenerated electrons to activate PMS. Moreover, the charge distributions in the model structures further indicated that a push/pull electron system formed in the ECN framework (Fig. 4a–b). The push/pull interactions could promote photogenerated charge separation, this well explained the PL quenching phenomena in ECN. These features of ECN were constructive to the persulfate activation under visible-light irradiation.

The PMS adsorption behavior over CN and ECN was theoretically investigated in detail. Fig. S7 showed that PMS was repelled by the catalyst and formed physical adsorption over CN, the adsorption energy is about -0.6 eV. This means that the PMS adsorption over CN was very weak. In the case of ECN (Fig. S8), the spatial structure of the catalyst was distorted and the charge density was delocalized when incorporating enol group into CN, which made the adsorption of PMS on ECN stronger. The optimized adsorption structure showed a good adsorption effect when the terminal H of the PMS was close to the N on the ECN, and the adsorption energy reached -1.3 eV. This was because hydrogen bond was formed between H atom of PMS and N atom of ECN. These results proved that ECN exhibited a better PMS adsorption capability.

In Table S2, the electron transfer values for PMS on CN and ECN were -0.967 and -0.987 e, respectively, further confirmed that PMS adsorbed more readily on ECN. Additionally, the prolonged bond length of O–O (lo-o) in PMS after adsorbing on ECN (1.469 Å) was larger than in CN (1.465 Å), indicating better PMS activation capabilities of ECN.

Fig. 4c–d also displays the higher deformation charge density of PMS after it adsorbed on ECN when compared to CN, implying that electrons transferred more easily between PMS and ECN. Moreover, we calculated the PMS activation pathways using transition state calculations. The energy barrier between the initial state (IS) and transition state (TS) was 1.85 eV over CN, while the value was 1.27 eV for ECN (Fig. 4e). This indicated that ECN had a lower energy barrier to overcome for PMS activation. Moreover, the final state (FS) energy was much lower than IS in the ECN system, implying that PMS activation on ECN was thermodynamically spontaneous. As a result, these outstanding characteristics would lead to the enhanced catalytic activity of PMS activation for organic degradation over ECN [52,53].

3.3. Comparison of different oxidation processes for BPA degradation

BPA degradation in different oxidation processes was measured to evaluate the catalytic performance of CN and ECN60. Firstly, BPA adsorption over the catalysts was investigated. In Fig. S9, both samples displayed similar adsorption capacity of BPA. This excluded the effect of BPA adsorption on their performance comparison. As shown in Fig. 5a, when only in the presence of PMS, the BPA removal rates were determined to be 7% and 34% after 30 min in the PMS/CN and PMS/ECN60 processes, respectively. This indicated that the incorporation of enol into the CN framework effectively activated PMS for BPA removal, which was consistent with the theoretical analysis results. Under visible-light irradiation, ECN60 showed better photocatalytic activity for BPA degradation (61%) than CN (13%), and this effect was ascribed to the enhanced light absorption and improved photogenerated charge carrier separation of ECN60. Interestingly, complete degradation of BPA was accomplished within 20 min in the Vis-PMS/ECN60 process, which was significantly better than the Vis-PMS/CN process. This also illustrated the markedly enhanced performance of ECN60 for activating PMS under visible-light irradiation. To evaluate the synergistic effect of different oxidation processes for BPA degradation, the rate constant was obtained from first-order kinetics. As shown in Fig. 5b, the constant of Vis-PMS/ECN60 process was 0.136 min⁻¹, which was as 3.4 times higher than the sum of the values for the Vis/ECN60 (0.031 min⁻¹) and PMS/ECN60 (0.0105 min⁻¹) processes. Therefore, the synergistic factor for ECN60 (3.37) is more prominent than the one for CN (1.38). These results confirmed that ECN60 displayed a significant synergy for BPA degradation in the presence of both visible-light irradiation and PMS. Similarly, the catalytic activity and the synergistic factor of other samples were also evaluated (Fig. S7a–d). Compared to CN, all ECN samples exhibited enhanced degradation of BPA and improved synergy, and ECN60 demonstrates the best performance. Moreover, 86% of the total organic carbon (TOC) was removed during the Vis-PMS/ECN60 process

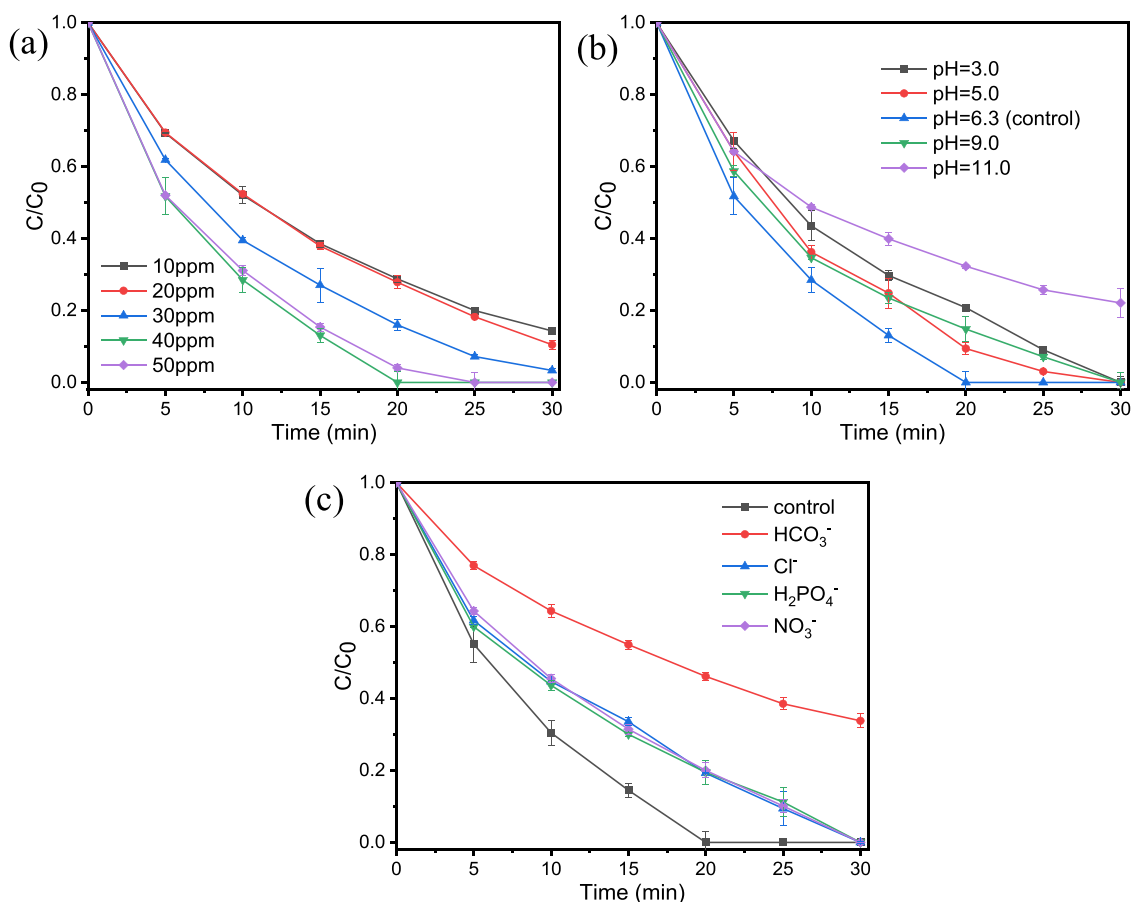


Fig. 6. Effect of (a) PMS concentration, (b) initial pH and (c) anions (1.0 mM) on BPA degradation. Reaction conditions: $[\text{PMS}] = 40 \text{ mg L}^{-1}$; $[\text{Catalyst}] = 0.33 \text{ g L}^{-1}$; $[\text{BPA}] = 20 \text{ mg L}^{-1}$; $T = 25^\circ \text{C}$.

after 30 min, which far exceeded that of the Vis-PMS/CN process (17%) (Fig. S7e). This value was also higher than the sum of the values in the Vis/ECN60 (46%) and PMS/ECN60 (17%) processes. Furthermore, the comparison between ECN60 and the reported photocatalysts were also summarized. As shown in Table S3, ECN60 exhibited an enhanced catalytic performance in BPA degradation under visible-light irradiation. All these results fully verified the excellent catalytic activity and the good synergy of the Vis-PMS/ECN process for the deep oxidation of BPA.

3.4. Influence of reaction parameters on the BPA degradation

The impact factors on BPA degradation during the is-PMS/ECN60 process were also examined. Fig. 6a shows BPA removal as a function of different concentrations of PMS ($0\text{--}50 \text{ mg L}^{-1}$). BPA degradation gradually accelerated as the PMS concentration increased from 0 to 40 mg L^{-1} . When the PMS concentration further increased to 50 mg L^{-1} , a slight decline in BPA removal was observed. This was due to the high concentration of PMS, which would impair the adsorption of BPA for the catalyst. The effect of solution pH is shown in Fig. 6b. The initial BPA solution ($\text{pH}=6.3$) exhibited optimal performance for BPA

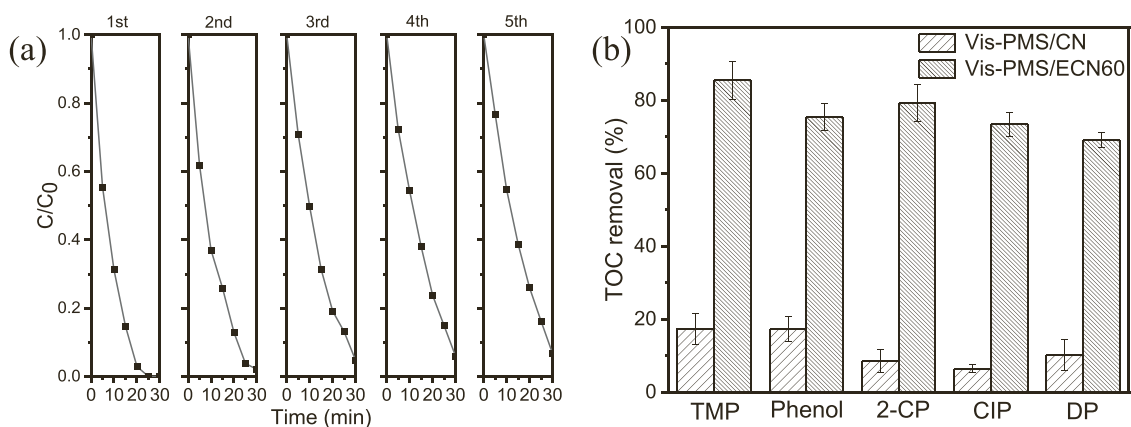


Fig. 7. (a) Reusability of ECN60 for BPA degradation and (b) TOC removal of the various organic compounds in the Vis-PMS/CN and Vis-PMS/ECN60 processes after 60 min. Reaction conditions: $[\text{PMS}] = 40 \text{ mg L}^{-1}$; $[\text{Catalyst}] = 0.33 \text{ g L}^{-1}$; $[\text{BPA}] = [\text{TMP}] = [\text{Phenol}] = [2\text{-CP}] = 20 \text{ mg L}^{-1}$; $[\text{CIP}] = [\text{DP}] = 10 \text{ mg L}^{-1}$; $T = 25^\circ \text{C}$.

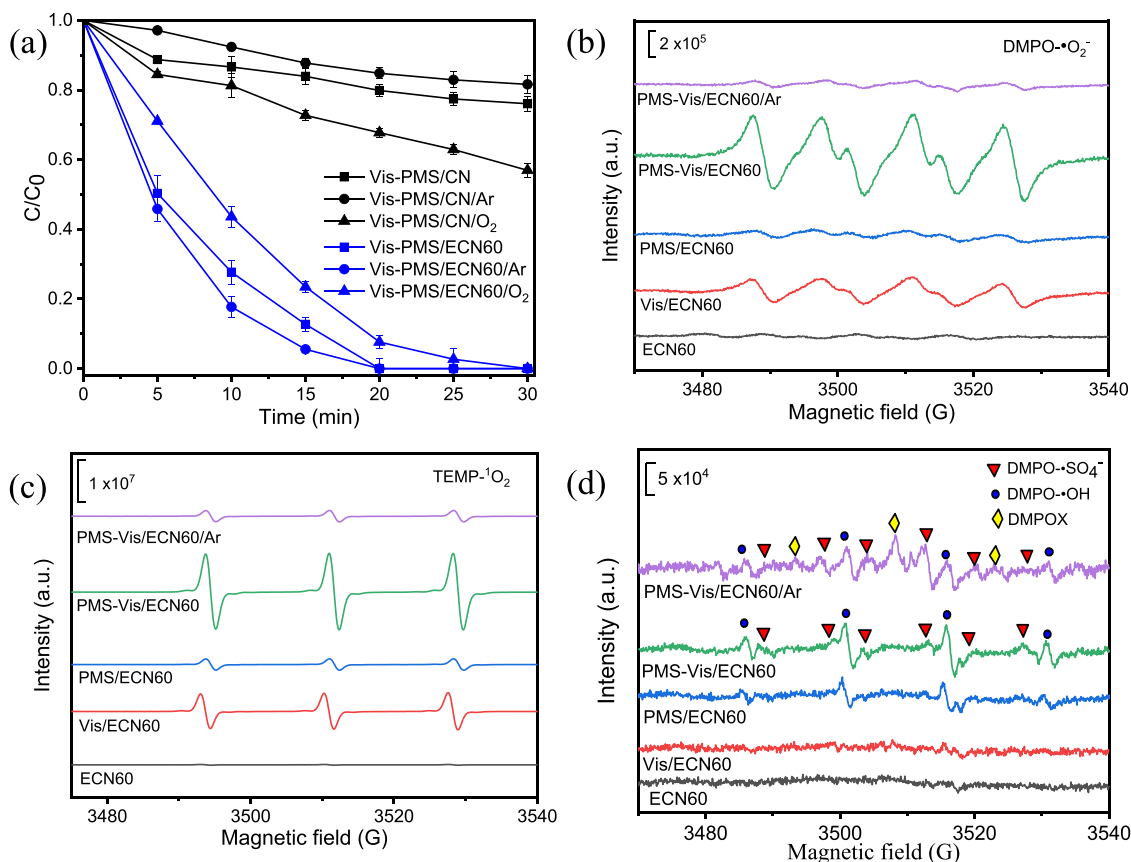


Fig. 8. (a) The BPA removal in the Vis-PMS/CN and Vis-PMS/ECN60 processes under different atmospheric conditions, reaction conditions: [PMS] = 40 mg L⁻¹; [Catalyst] = 0.33 g L⁻¹; [BPA] = 20 mg L⁻¹; T = 25 °C. (b-d) Spin-trapping EPR spectra for •O₂⁻, ¹O₂ and •OH/•SO₄⁻ in the different processes.

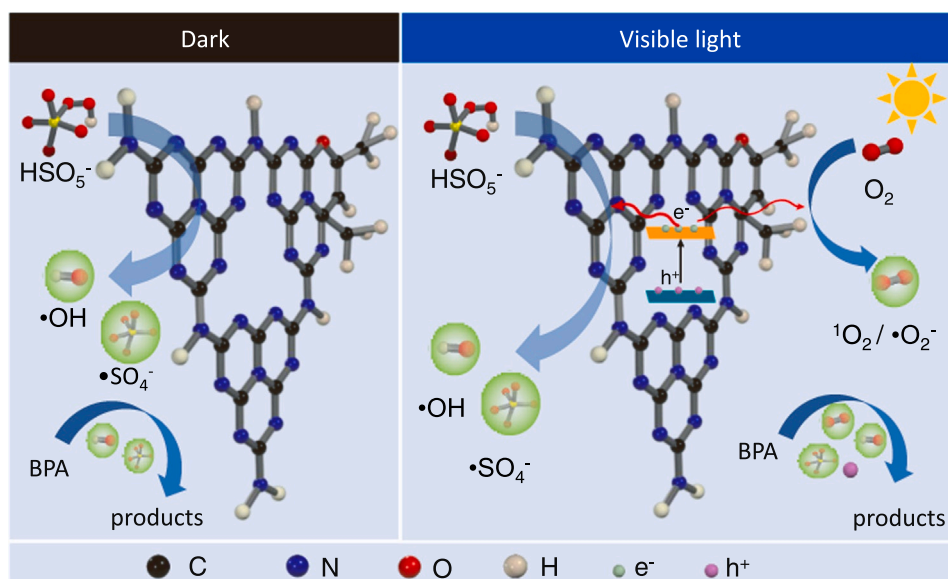
degradation, while acidic and alkaline conditions were unfavorable for the reaction. When the initial pH of the solution was adjusted from 3.0 to 6.3, the increase in OH⁻ promoted PMS activation. The point of zero charge (PZC) for ECN60 was 7.6 (Fig. S8), indicating a negatively charged ECN60 surface when the solution pH was greater than 7.6. In this case, the negatively charged ECN60 surface would block the adsorption of HSO₅⁻ because of the electrostatic repulsion, which affected the activation of HSO₅⁻ and reactive oxygen species (ROS) production, resulting in poor BPA degradation efficiency in the high pH solution [54]. Various inorganic anions, include HCO₃⁻, Cl⁻, H₂PO₄⁻ and NO₃⁻ were considered for water decontamination. As shown in Fig. 6c, the addition of Cl⁻, H₂PO₄⁻ or NO₃⁻ had a certain degree of influence on BPA degradation, because the PZC was higher than the initial pH of the system. The positively charged surface would adsorb anions and restrict the activation of HSO₅⁻. Moreover, when HCO₃⁻ was introduced into the solution and just 66% of BPA was removed in 30 min. This was ascribed to the fact that produced ROS was readily scavenged by HCO₃⁻ during the advanced oxidation process [55].

The catalytic stability of ECN60 during the Vis-PMS process was also evaluated using a cyclic test. As shown in Fig. 7a, no significant declines in catalytic performance were observed during the cyclic runs, and as much as 94% of BPA was removed after five runs. Moreover, the XRD patterns, FTIR spectra, and SEM images of used ECN60 were similar to fresh ECN60 (Fig. S9), suggesting the robust reusability of ECN60. The suitability of the Vis-PMS/ECN60 process was also assessed by degrading BPA in deionized water, lake water, and tap water. The results (Fig. S10) showed that BPA elimination was minimally affected by the water type. Moreover, we also assessed the degradation of other organic pollutants such as phenol, 2-chlorophenol (2-CP), Trimethoprim (TMP), Ciprofloxacin (CIP), and Diphenhydramine (DP), to investigate the universality of the Vis-PMS/ECN60 process. As shown in Fig. 7b, high

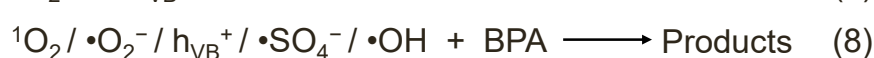
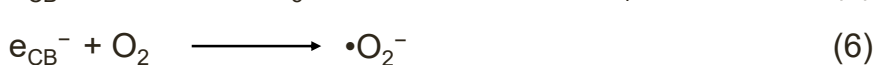
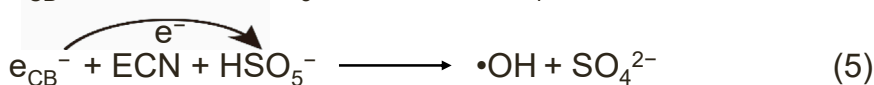
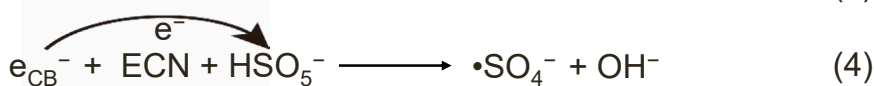
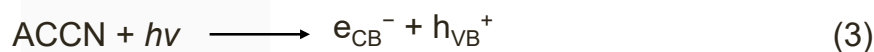
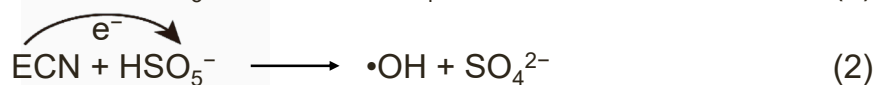
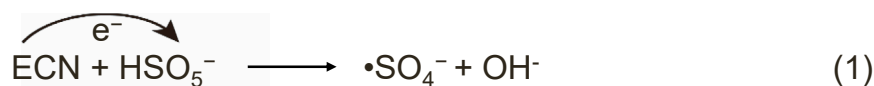
TOC removal rates in 60 min were also achieved for these organic removal. These results demonstrated that ECN60 possessed good reusability and potential for actual water decontamination application.

3.5. A mechanism in the catalytic process

To determine the source of ROS in the different oxidation processes, Ar was introduced into the oxidation process to remove the dissolved O₂ in the reaction system and the results are shown in Fig. S11. For the Vis/ECN60 process, BPA was barely removed under Ar-saturated conditions. This indicated that the main ROS (•O₂⁻ and ¹O₂) in the Vis/ECN60 process was from O₂. For the PMS/ECN60 process, the introduction of Ar slightly increased the BPA degradation, this meant that the ROS were mainly due to PMS activation from the catalyst and the dissolved oxygen possibly affected the PMS activation in the dark [56,57]. Surprisingly, better performance of BPA degradation was achieved in the Vis-PMS/ECN60 process under Ar-saturated conditions than atmospheric air (Fig. 8a). To reveal the principle of this phenomenon, pure oxygen was bubbled into the reaction solution during the Vis-PMS/ECN60 process, and we found that the catalytic activity significantly decreased. Based on these results, it could be concluded that O₂ activation and PMS activation completed each other in the Vis-PMS/ECN60 process. For comparison, we also investigated the Vis-PMS/CN process under different atmospheric conditions. As shown in Fig. 5a, the introduction of O₂ promoted the removal rate of BPA during the Vis-PMS/CN process, while the Ar-saturated conditions were unfavorable for BPA degradation. As indicated by the DFT calculation results, ECN showed better PMS absorption performance than CN, and the photogenerated electrons preferentially transferred to the adsorbed PMS and numerous strong-oxidizing •SO₄⁻ were produced, which accelerated BPA degradation in the Vis-PMS/ECN60/Ar process. This



Scheme 2. PMS activation mechanism over ECN catalyst.



would be useful for wastewater treatment under anaerobic conditions. Furthermore, changes in PMS concentrations during the reaction were also monitored [58]. As shown in Fig. S12, the PMS concentration decreased with prolonged reaction time. After reacting for 30 min, the residual concentrations were 26, 21 and 11 mg L⁻¹ in the oxygen-, air- and Ar-atmospheres, respectively. This also confirmed that there was competition between the PMS and dissolved O₂ for capturing photo-generated electrons, which affected the amount and type of produced ROS for organic degradation.

ROS production generated under different conditions was measured using EPR with 5,5-Dimethyl-1-Pyrroline-N-Oxide (DMPO) and 2,2,6,6-tetramethylpiperidine (TEMP) as radical spin trapping agents [59]. As shown in Fig. 8b–d, characteristic EPR signals assigned to •O₂⁻ and ¹O₂ were observed in the Vis/ECN60 process, and the signals for •SO₄⁻, •OH and ¹O₂ were detected in the PMS/ECN60 process. The signals for these four kinds of active species significantly strengthened in the Vis-PMS/ECN60 process. This indicates that PMS could be efficiently activated by the photogenerated electrons in the photocatalytic process.

Interestingly, under Ar-saturated condition, the signal intensities for •OH, •O₂⁻ and ¹O₂ were greatly reduced, but the signal for •SO₄⁻ was enhanced. Furthermore, three new peaks, marked with yellow symbols, were possibly due to DMPO which was oxidized by excess •SO₄⁻ [54]. Therefore, we inferred that •SO₄⁻ was the major ROS in the Vis-PMS/ECN60/Ar system and contributed to its enhanced performance for BPA degradation.

Based on the above results, we proposed a mechanism for the reaction. As illustrated in Scheme 2, the mechanism involved in PMS activation in the dark and photo-assisted PMS activation. (i) On the surface of ECN, adsorbed PMS was activated by the electrons in electron-rich region, generating •SO₄⁻ and •OH during the PMS/ECN process (Eqs. (1–2)). However, this reaction was restricted if the consumed electrons were not replenished in time. (ii) After irradiation with visible-light irradiation, ECN was excited and produced photogenerated electrons on the conduction band (CB) and holes on the valence band (VB) (Eq. (3)), then the photogenerated electrons could constantly supplement to drive the processes (Eqs. (4–5)). Moreover, the photogenerated electrons

also activated the dissolved O_2 in the solution, generating 1O_2 and $\bullet O_2^-$ (Eqs. 6–7). Finally, BPA was degraded by the above-mentioned ROS attack (Eq. (8)).

4. Conclusions

This study demonstrated that the incorporation of enol into the polyheptazine based CN network effectively tailored its electronic structure. This benefited from the delocalization of π -electrons by incorporating enol, and PMS could easily adsorb on ECN. Then the photogenerated electrons rapidly and preferentially transferred to the adsorbed PMS. As a result, PMS was efficiently activated and generated $\bullet SO_4^-$, which had a strong oxidation ability for organic contaminant degradation in the Vis-PMS/ECN process. This study presented a photo-assisted persulfate-based oxidation process for environmental purification. Additionally, the metal-free materials obtained using this facile method behaved as green PMS activator and photocatalyst, and could efficiently activate PMS for organic pollutant removal under visible-light irradiation, especially under anaerobic conditions. This might offer some guidelines for designing and synthesizing appropriate catalysts for visible-light-driven persulfate activation for organic wastewater treatment.

CRediT authorship contribution statement

Hongbo Ming: Conceptualization, Methodology, Investigation, Writing – original draft. **Peiyun Zhang:** Investigation, Validation. **Yang Yang:** Data curation, Validation. **Yu Zou:** Software, Validation. **Can Yang:** Data curation, Resources. **Yidong Hou:** Resources, Conceptualization, Project administration, Supervision, Writing – review & editing. **Kaining Ding:** Software, Supervision, Writing – review & editing. **Jinshui Zhang:** Writing – review & editing, Supervision. **Xinchun Wang:** Resources, Supervision, Writing – review & editing.

Declaration of Competing Interest

The authors declare no competing financial interest.

Acknowledgement

The work was supported by NSFC (22072021, U1805255, U1905214, 21972022), and National Key Technologies R&D Program of China (2018YFA0209301, 2014BAC13B03).

Appendix A. Supporting information

Supplementary data associated with this article can be found in the online version at [doi:10.1016/j.apcatb.2022.121341](https://doi.org/10.1016/j.apcatb.2022.121341).

References

- G.P. Anipsitakis, D.D. Dionysiou, M.A. Gonzalez, Cobalt-mediated activation of peroxymonosulfate and sulfate radical attack on phenolic compounds. Implications of chloride ions, *Environ. Sci. Technol.* 40 (2006) 1000–1007, <https://doi.org/10.1021/es050634b>.
- Z. Cai, A.D. Dwivedi, W.-N. Lee, X. Zhao, W. Liu, M. Sillanpää, D. Zhao, C.-H. Huang, J. Fu, Application of nanotechnologies for removing pharmaceutically active compounds from water: development and future trends, *Environ. Sci. Nano* 5 (2018) 27–47, <https://doi.org/10.1039/C7EN00644F>.
- J. Lee, U. Von Gunten, J.-H. Kim, Persulfate-based advanced oxidation: critical assessment of opportunities and roadblocks, *Environ. Sci. Technol.* 54 (2020) 3064–3081, <https://doi.org/10.1021/acs.est.9b07082>.
- H.H. Gao, H.C. Yang, J.Z. Xu, S.W. Zhang, J.X. Li, Strongly coupled g-C₃N₄ nanosheets-Co₃O₄ quantum dots as 2D/0D heterostructure composite for peroxymonosulfate activation, *Small* 14 (2018), e1801353, <https://doi.org/10.1002/sml.201801353>.
- R.L. Johnson, P.G. Tratnyek, R.O. Johnson, Persulfate persistence under thermal activation conditions, *Environ. Sci. Technol.* 42 (2008) 9350–9356, <https://doi.org/10.1021/es8019462>.
- G. Ayoub, A. Ghauch, Assessment of bimetallic and trimetallic iron-based systems for persulfate activation: application to sulfamethoxazole degradation, *Chem. Eng. J.* 256 (2014) 280–292, <https://doi.org/10.1016/j.cej.2014.07.002>.
- H. Milh, D. Cabooter, R. Dewil, Role of process parameters in the degradation of sulfamethoxazole by heat-activated peroxymonosulfate oxidation: radical identification and elucidation of the degradation mechanism, *Chem. Eng. J.* 422 (2021), 130457, <https://doi.org/10.1016/j.cej.2021.130457>.
- C. Cai, H. Zhang, X. Zhong, L.W. Hou, Ultrasound enhanced heterogeneous activation of peroxymonosulfate by a bimetallic Fe-Co/SBA-15 catalyst for the degradation of Orange II in water, *J. Hazard. Mater.* 283 (2015) 70–79, <https://doi.org/10.1016/j.jhazmat.2014.08.053>.
- F. Ghanbari, M. Khatibasreh, M. Mahdavianpour, K.Y.A. Lin, Oxidative removal of benzotriazole using peroxymonosulfate/ultrasound: synergy, optimization, degradation intermediates and utilizing for real wastewater, *Chemosphere* 244 (2020), 125326, <https://doi.org/10.1016/j.chemosphere.2019.125326>.
- S.D. Yan, Y. Shi, Y.F. Tao, H. Zhang, Enhanced persulfate-mediated photocatalytic oxidation of bisphenol A using bioelectricity and a g-C₃N₄/Fe₂O₃ heterojunction, *Chem. Eng. J.* 359 (2019) 933–943, <https://doi.org/10.1016/j.cej.2018.11.093>.
- Y.N. Liu, R.X. Qu, X.Y. Li, Y. Wei, L. Feng, A bifunctional beta-MnO₂ mesh for expeditious and ambient degradation of dyes in activation of peroxymonosulfate (PMS) and simultaneous oil removal from water, *J. Colloid Interface Sci.* 579 (2020) 412–424, <https://doi.org/10.1016/j.jcis.2020.06.073>.
- J. Yang, M. Zhu, D.D. Dionysiou, What is the role of light in persulfate-based advanced oxidation for water treatment? *Water Res.* 189 (2021), 116627, <https://doi.org/10.1016/j.watres.2020.116627>.
- Y. Gong, X. Zhao, H. Zhang, B. Yang, K. Xiao, T. Guo, J. Zhang, H. Shao, Y. Wang, G. Yu, MOF-derived nitrogen doped carbon modified g-C₃N₄ heterostructure composite with enhanced photocatalytic activity for bisphenol A degradation under peroxymonosulfate under visible light irradiation, *Appl. Catal. B Environ.* 233 (2018) 35–45, <https://doi.org/10.1016/j.apcatb.2018.03.077>.
- F. Chen, G.-X. Huang, F.-B. Yao, Q. Yang, Y.-M. Zheng, Q.-B. Zhao, H.-Q. Yu, Catalytic degradation of ciprofloxacin by a visible-light-assisted peroxymonosulfate activation system: Performance and mechanism, *Water Res.* 173 (2020), 115559, <https://doi.org/10.1016/j.watres.2020.115559>.
- M. Ding, W. Ao, H. Xu, W. Chen, L. Tao, Z. Shen, H. Liu, C. Lu, Z. Xie, Facile construction of dual heterojunction CoO@TiO₂/MXene hybrid with efficient and stable catalytic activity for phenol degradation with peroxymonosulfate under visible light irradiation, *J. Hazard. Mater.* 420 (2021), 126686, <https://doi.org/10.1016/j.jhazmat.2021.126686>.
- A.Q. Wang, Z. Chen, Z.K. Zheng, H. Xu, H. Wang, K. Hu, K. Yan, Remarkably enhanced sulfate radical-based photo-Fenton-like degradation of levofloxacin using the reduced mesoporous MnO@MnO_x microspheres, *Chem. Eng. J.* 379 (2020), 122340, <https://doi.org/10.1016/j.cej.2019.122340>.
- L. Wang, X. Huang, M. Han, L. Lyu, T. Li, Y. Gao, Q. Zeng, C. Hu, Efficient inhibition of photogenerated electron-hole recombination through persulfate activation and dual-pathway degradation of micropollutants over iron molybdate, *Appl. Catal. B Environ.* 257 (2019), 117904, <https://doi.org/10.1016/j.apcatb.2019.117904>.
- H.X. Shao, Y.B. Wang, H.B. Zeng, J.J. Zhang, Y. Wang, M. Sillanpää, X. Zhao, Enhanced photoelectrocatalytic degradation of bisphenol A by BiVO₄ photoanode coupling with peroxymonosulfate, *J. Hazard. Mater.* 394 (2020), 121105, <https://doi.org/10.1016/j.jhazmat.2019.121105>.
- H. Guo, H.Y. Niu, C. Liang, C.G. Niu, Y. Liu, N. Tang, Y. Yang, H.Y. Liu, Y.Y. Yang, W.J. Wang, Few-layer graphitic carbon nitride nanosheet with controllable functionalization as an effective metal-free activator for peroxymonosulfate photocatalytic activation: role of the energy band bending, *Chem. Eng. J.* 401 (2020), 126072, <https://doi.org/10.1016/j.cej.2020.126072>.
- H.B. Ming, D.L. Wei, Y. Yang, B.Q. Chen, C. Yang, J.S. Zhang, Y.D. Hou, Photocatalytic activation of peroxymonosulfate by carbon quantum dots functionalized carbon nitride for efficient degradation of bisphenol A under visible-light irradiation, *Chem. Eng. J.* 424 (2021), 130296, <https://doi.org/10.1016/j.cej.2021.130296>.
- Y. Yang, X. Li, C.Y. Zhou, W.P. Xiong, G.M. Zeng, D.L. Huang, C. Zhang, W. J. Wang, B.A. Song, X. Tang, X.P. Li, H. Guo, Recent advances in application of graphitic carbon nitride-based catalysts for degrading organic contaminants in water through advanced oxidation processes beyond photocatalysis: a critical review, *Water Res.* 184 (2020), 116200, <https://doi.org/10.1016/j.watres.2020.116200>.
- J.S. Zhang, B. Wang, X.C. Wang, Chemical synthesis and applications of graphitic carbon Nitride, *Acta Phys. Chim. Sin.* 29 (9) (2013) 1865–1876, 10.3866/PKU.WHXB201306173.
- L.L. Wang, X. Guo, Y.Y. Chen, S.S. Ai, H.M. Ding, Cobalt-doped g-C₃N₄ as a heterogeneous catalyst for photo-assisted activation of peroxymonosulfate for the degradation of organic contaminants, *Appl. Surf. Sci.* 467 (2019) 954–962, <https://doi.org/10.1016/j.apsusc.2018.10.262>.
- R.B. Li, M.X. Cai, Z.J. Xie, Q.X. Zhang, Y.Q. Zeng, H.J. Liu, G.G. Liu, W.Y. Lv, Construction of heterostructured CuFe₂O₄/g-C₃N₄ nanocomposite as an efficient visible light photocatalyst with peroxysulfate for the organic oxidation, *Appl. Catal. B Environ.* 244 (2019) 974–982, <https://doi.org/10.1016/j.apcatb.2018.12.043>.
- F. Guo, X.L. Huang, Z.H. Chen, H.R. Sun, L.Z. Chen, Prominent co-catalytic effect of CoP nanoparticles anchored on high-crystalline g-C₃N₄ nanosheets for enhanced visible-light photocatalytic degradation of tetracycline in wastewater, *Chem. Eng. J.* 395 (2020), 125118, <https://doi.org/10.1016/j.cej.2020.125118>.
- J. Miao, W. Geng, P.J.J. Alvarez, M.C. Long, 2D N-doped porous carbon derived from polydopamine-coated graphitic carbon nitride for efficient nonradical

- activation of peroxymonosulfate, *Environ. Sci. Technol.* 54 (13) (2020) 8473–8481, <https://doi.org/10.1021/acs.est.0c03207>.
- [27] S. Zhang, S. Song, P.C. Gu, R. Ma, D.L. Wei, G.X. Zhao, T. Wen, R. Jehan, B.W. Hu, X.K. Wang, Visible-light-driven activation of persulfate over cyano and hydroxyl group co-modified mesoporous g-C₃N₄ for boosting bisphenol A degradation, *J. Mater. Chem. A* 7 (10) (2019) 5552–5560, <https://doi.org/10.1039/C9TA00339H>.
- [28] S. She, Y. Wang, R. Chen, F. Yi, C. Sun, J. Hu, Z. Li, G. Lu, M. Zhu, Ultrathin S-doped graphitic carbon nitride nanosheets for enhanced sulpiride degradation via visible-light-assisted peroxydisulfate activation: performance and mechanism, *Chemosphere* 266 (2021), 128929 <https://doi.org/10.1016/j.chemosphere.2020.128929>.
- [29] X.P. Zong, L.J. Niu, W.S. Jiang, Y.M. Yu, L. An, D. Qu, X.Y. Wang, Z.C. Sun, Constructing creatinine-derived moiety as donor block for carbon nitride photocatalyst with extended absorption and spatial charge separation, *Appl. Catal. B Environ.* 291 (2021), 120099, <https://doi.org/10.1016/j.apcatb.2021.120099>.
- [30] W. Che, W. Cheng, T. Yao, F. Tang, W. Liu, H. Su, Y. Huang, Q. Liu, J. Liu, F. Hu, Z. Pan, Z. Sun, S. Wei, Fast photoelectron transfer in (Cring)-C₃N₄ plane heterostructural nanosheets for overall water splitting, *J. Am. Chem. Soc.* 139 (8) (2017) 3021–3026, <https://doi.org/10.1021/jacs.6b11878>.
- [31] P.X. Qiu, C.M. Xu, H. Chen, F. Jiang, X. Wang, R.F. Lu, X.R. Zhang, One step synthesis of oxygen doped porous graphitic carbon nitride with remarkable improvement of photo-oxidation activity: Role of oxygen on visible light photocatalytic activity, *Appl. Catal. B Environ.* 206 (2017) 319–327, <https://doi.org/10.1016/j.apcatb.2017.01.058>.
- [32] S. Zhang, Y. Liu, P.C. Gu, R. Ma, T. Wen, G.X. Zhao, L. Li, Y.J. Ai, C. Hu, X.K. Wang, Enhanced photodegradation of toxic organic pollutants using dual-oxygen-doped porous g-C₃N₄: Mechanism exploration from both experimental and DFT studies, *Appl. Catal. B Environ.* 248 (2019) 1–10, <https://doi.org/10.1016/j.apcatb.2019.02.008>.
- [33] J.H. Li, B.A. Shen, Z.H. Hong, B.Z. Lin, B.F. Gao, Y.L. Chen, A facile approach to synthesize novel oxygen-doped g-C₃N₄ with superior visible-light photoreactivity, *Chem. Commun.* 48 (98) (2012) 12017–12019, <https://doi.org/10.1039/C2CC35862J>.
- [34] Y.W. Gao, Y. Zhu, L. Lyu, Q.Y. Zeng, X.C. Xing, C. Hu, Electronic structure modulation of graphitic carbon nitride by oxygen doping for enhanced catalytic degradation of organic pollutants through peroxymonosulfate activation, *Environ. Sci. Technol.* 52 (24) (2018) 14371–14380, <https://doi.org/10.1021/acs.est.8b05246>.
- [35] C.-Q. Xu, W.-D. Zhang, K. Deguchi, S. Ohki, T. Shimizu, R. Ma, T. Sasaki, Construction of a push–pull system in g-C₃N₄ for efficient photocatalytic hydrogen evolution under visible light, *J. Mater. Chem. A* 8 (26) (2020) 13299–13310, <https://doi.org/10.1039/C9TA13513H>.
- [36] B. Delley, From molecules to solids with the DMol(3) approach, *J. Chem. Phys.* 113 (2000) 7756–7764, <https://doi.org/10.1063/1.1316015>.
- [37] J.P. Perdew, K. Burke, M. Ernzerhof, Generalized gradient approximation made simple, *Phys. Rev. Lett.* 77 (1996) 3865–3868, <https://doi.org/10.1103/PhysRevLett.77.3865>.
- [38] A.M. Schmiedekamp, I.A. Topol, S.K. Burt, et al., Triazene proton affinities: a comparison between density functional, Hartree-Fock, and post-Hartree-Fock methods, *J. Comput. Chem.* 15 (1994) 875–892, <https://doi.org/10.1002/jcc.540150809>.
- [39] X. Wang, K. Maeda, X. Chen, K. Takanabe, K. Domen, Y. Hou, X. Fu, M. Antonietti, Polymer semiconductors for artificial photosynthesis: hydrogen evolution by mesoporous graphitic carbon nitride with visible light, *J. Am. Chem. Soc.* 131 (5) (2009) 1680–1681, <https://doi.org/10.1021/ja809307s>.
- [40] Y. Li, C. Zhang, D. Shuai, S. Naraginti, D. Wang, W. Zhang, Visible-light-driven photocatalytic inactivation of MS₂ by metal-free g-C₃N₄: virucidal performance and mechanism, *Water Res.* 106 (2016) 249–258, <https://doi.org/10.1016/j.watres.2016.10.009>.
- [41] W. Chen, T. Huang, Y.-X. Hua, T.-Y. Liu, X.-H. Liu, S.-M. Chen, Hierarchical CdIn₂S₄ microspheres wrapped by mesoporous g-C₃N₄ ultrathin nanosheets with enhanced visible light driven photocatalytic reduction activity, *J. Hazard. Mater.* 320 (2016) 529–538, <https://doi.org/10.1016/j.jhazmat.2016.08.025>.
- [42] B.H. Long, J.L. Lin, X.C. Wang, Thermally-induced desulfurization and conversion of guanidine thiocyanate into graphitic carbon nitride catalysts for hydrogen photosynthesis, *J. Mater. Chem. A* 2 (9) (2014) 2942–2951, <https://doi.org/10.1039/C3TA14339B>.
- [43] Y. Duan, L. Deng, Z. Shi, X. Liu, H. Zeng, H. Zhang, J. Crittenden, Efficient sulfadiazine degradation via in-situ epitaxial grow of graphitic carbon nitride (g-C₃N₄) on carbon dots heterostructures under visible light irradiation: synthesis, mechanisms and toxicity evaluation, *J. Colloid Interface Sci.* 561 (2020) 696–707, <https://doi.org/10.1016/j.jcis.2019.11.046>.
- [44] Y. Wang, H. Wang, F. Chen, F. Cao, X. Zhao, S. Meng, Y. Cui, Facile synthesis of oxygen doped carbon nitride hollow microsphere for photocatalysis, *Appl. Catal. B Environ.* 206 (2017) 417–425, <https://doi.org/10.1016/j.apcatb.2017.01.041>.
- [45] J. Sun, J. Zhang, M. Zhang, M. Antonietti, X. Fu, X. Wang, Bioinspired hollow semiconductor nanospheres as photosynthetic nanoparticles, *Nat. Commun.* 3 (1) (2012) 1139, <https://doi.org/10.1038/ncomms2152>.
- [46] D.W. Sendorf, G.E. Maciel, Carbon-13 CP/MAS NMR study of molecular motion in n-alkylsilane bonded to the silica surface, *J. Am. Chem. Soc.* 105 (7) (1983) 1848–1851, <https://doi.org/10.1002/chin.198328050>.
- [47] N. Kamiya, M. Sakurai, Y. Inoue, R. Chujo, Y. Doi, Study of cocrystallization of poly (3-hydroxybutyrate-co-3-hydroxyvalerate) by solid-state high-resolution carbon-13 NMR spectroscopy and differential scanning calorimetry, *Macromolecules* 24 (9) (1991) 2178–2182, <https://doi.org/10.1021/ma00009a006>.
- [48] D.-S. Kong, The influence of fluoride on the physicochemical properties of anodic oxide films formed on titanium surfaces, *Langmuir* 24 (10) (2008) 5324–5331, <https://doi.org/10.1021/la703258e>.
- [49] J.S. Zhang, X.F. Chen, K. Takanabe, K. Maeda, K. Domen, J.D. Epping, X.Z. Fu, M. Antonietti, X.C. Wang, Synthesis of a carbon nitride structure for visible-light catalysis by copolymerization, *Angew. Chem. Int. Ed.* 49 (2) (2010) 441–444, <https://doi.org/10.1002/anie.200903886>.
- [50] H. Shi, S. Long, J. Hou, L. Ye, Y. Sun, W. Ni, C. Song, K. Li, G.G. Gurzadyan, X. Guo, Defects promote ultrafast charge separation in graphitic carbon nitride for enhanced visible-light-driven CO₂ reduction activity, *Chem. Eur. J.* 25 (19) (2019) 5028–5035, <https://doi.org/10.1002/chem.201805923>.
- [51] X.L. Wang, H.G. Yang, Facile fabrication of high-yield graphitic carbon nitride with a large surface area using bifunctional urea for enhanced photocatalytic performance, *Appl. Catal. B Environ.* 205 (2017) 624–630, <https://doi.org/10.1016/j.apcatb.2017.01.013>.
- [52] J.L. Zhang, B.H. Jing, Z.Y. Tang, Z.M. Ao, D.H. Xia, M.S. Zhu, S.B. Wang, Experimental and DFT insights into the visible-light driving metal-free C₃N₅ activated persulfate system for efficient water purification, *Appl. Catal. B Environ.* 289 (2021), 120023, <https://doi.org/10.1016/j.apcatb.2021.120023>.
- [53] W.J. Liu, C.Y. Nie, W.L. Li, Z.M. Ao, S.B. Wang, T.C. An, Oily sludge derived carbons as peroxymonosulfate activators for removing aqueous organic pollutants: Performances and the key role of carbonyl groups in electron-transfer mechanism, *J. Hazard. Mater.* 414 (2021), 125552 <https://doi.org/10.1016/j.jhazmat.2021.125552>.
- [54] L.J. Xu, L.Y. Qi, Y. Sun, H. Gong, Y.L. Chen, C. Pei, L. Gan, Mechanistic studies on peroxymonosulfate activation by g-C₃N₄ under visible light for enhanced oxidation of light-inert dimethyl phthalate, *Chin. J. Catal.* 41 (2) (2020) 322–332, [https://doi.org/10.1016/S1872-2067\(19\)63447-9](https://doi.org/10.1016/S1872-2067(19)63447-9).
- [55] A. Ghauch, A. Tuqan, N. Kibbi, Naproxen abatement by thermally activated persulfate in aqueous systems, *Chem. Eng. J.* 279 (2015) 861–873, <https://doi.org/10.1016/j.cej.2015.05.067>.
- [56] H. Guo, H.Y. Niu, C. Liang, C.G. Niu, Y. Liu, N. Tang, Y. Yang, H.Y. Liu, Y.Y. Yang, W.J. Wang, Few-layer graphitic carbon nitride nanosheet with controllable functionalization as an effective metal-free activator for peroxymonosulfate photocatalytic activation: role of the energy band bending, *Chem. Eng. J.* 401 (2020), 126072, <https://doi.org/10.1016/j.cej.2020.126072>.
- [57] Y.W. Gao, Y. Zhu, T. Li, Z.H. Chen, Q.K. Jiang, Z.Y. Zhao, X.Y. Liang, C. Hu, Unraveling the high-activity origin of single-atom iron catalysts for organic pollutant oxidation via peroxymonosulfate activation, *Environ. Sci. Technol.* 55 (12) (2021) 8318, <https://doi.org/10.1021/acs.est.1c01131>.
- [58] S. Wacławek, K. Grubel, M. Cernik, Simple spectrophotometric determination of monopersulfate, *Spectrochim. Acta Part A Mol. Bio Mol. Spectrosc.* 149 (2015) 928–933, <https://doi.org/10.1016/j.saa.2015.05.029>.
- [59] K. Rangelova, A.B. Rice, A. Khajo, M. Triquigneaux, S. Garantziotis, R. S. Magliozzo, R.P. Mason, Formation of reactive sulfite-derived free radicals by the activation of human neutrophils: an ESR study, *Free Radic. Biol. Med.* 52 (8) (2012) 1264–1271, <https://doi.org/10.1016/j.freeradbiomed.2012.01.016>.